

KBF₄ Additive for Alleviating Microstrain, Improving Crystallinity, and Passivating Defects in Inverted Perovskite Solar Cells

Haiyang Cheng, Chunki Liu, Jing Zhuang, Jiupeng Cao, Tianyue Wang, Wai-Yeung Wong, and Feng Yan*

Triple-cation mixed perovskites have attracted much attention recently owing to their prominent optoelectronic properties and good stability for perovskite solar cells. However, the introduction of those cations with different sizes in the perovskite materials will drive the perovskite lattice away from ideal cubic structure and lead to microstrain in the resultant films. Herein, a small amount of KBF₄ as an additive to elevate the quality of triple-cation mixed perovskite thin films is introduced. It is found that KBF₄ can enhance the crystallinity and alleviate microstrain of the perovskite thin films. Moreover, KBF₄ can passivate defects in perovskite grains, leading to much longer carrier lifetimes. Consequently, the resultant devices show improved fill factor, enhanced device efficiency, and better device stability. Under optimum fabrication conditions, triple-cation mixed perovskite solar cells with an inverted structure show power conversion efficiency over 23% as well as excellent stability under different conditions.

1. Introduction

The skyrocketing power conversion efficiency (PCE) of organic–inorganic halide perovskite solar cells (PSCs) has enabled them to be the most promising next-generation photovoltaic technology. The merits, such as tunable semiconducting properties, relatively easy processing methods, and inexpensive raw materials endow PSCs great potentials for commercialization.^[1,2]

H. Cheng, C. Liu, J. Zhuang, J. Cao, T. Wang, F. Yan
Department of Applied Physics
The Hong Kong Polytechnic University
Kowloon, Hong Kong, P. R. China
E-mail: apafyan@polyu.edu.hk

W.-Y. Wong
Department of Applied Biology & Chemical Technology and Research
Institute for Smart Energy
The Hong Kong Polytechnic University
Kowloon, Hong Kong, P. R. China

W.-Y. Wong, F. Yan
Research Institute of Intelligent Wearable Systems
The Hong Kong Polytechnic University
Hung Hom, Kowloon, Hong Kong SAR 999077, P. R. China

 The ORCID identification number(s) for the author(s) of this article can be found under <https://doi.org/10.1002/adfm.202204880>.

DOI: 10.1002/adfm.202204880

Numerous efforts have been devoted to enhance the device performance, including compositional engineering,^[3] interface engineering,^[4] and additive engineering.^[5,6] For various perovskite compositions, formamidinium (FA)-based PSCs have delivered many record efficiencies owing to their high short circuit current density (J_{sc}) brought by the broad light absorption spectra.^[7] However, FA-based perovskite has an unstable black α -phase and can easily undergo a phase transition from black α -phase to photo-inactivated-phase below 150 °C. Multiple strategies had been put forward to tackle the unstable black α -phase. For instance, various additives, such as methylammonium thiocyanate (MASCN),^[8] formamidinium formate (FAHCOO),^[9] and isopropylammonium chloride (IPACl)^[10]

have been introduced into FA-based perovskites with promising effects.

For compositional engineering, one of the strategy is to add a small amount of other A site cations such as MA⁺ (methylammonium) and Cs⁺ (cesium) to stabilize the black α -phase by entropic stabilization effect without compromising the high J_{sc} .^[11,12] By adopting a triple-cation system, a stable black α -phase could be achieved under a much lower temperature (100 °C).^[13] Moreover, the carrier lifetimes and transportation efficiency in a triple-cation system were also reported to be much longer and higher as compared to traditional double or single cation system.^[13] Although great efforts have been devoted to further enhance the performance of triple-cation based PSCs, many issues remain challenging. For example, the incorporation of A site cations with different size will lead to an increase of microstrain because of the distortion of the ideal structure.^[14] Such microstrain may lead to defects and consequently nonradiative recombination, which will severely compromise the device efficiency and stability.^[15,16]

The device structure of PSCs could be generally classified into normal n-i-p type and inverted p-i-n type. Although the record efficiency for PSCs has been achieved in the normal type,^[7] the inverted PSCs are even more popular in practical applications such as tandem solar cells,^[17] flexible electronics,^[18] and large-area devices by blade coating.^[19] However, the fabrication of inverted PSCs with high efficiency is more challenging.^[20]

Herein, we develop a convenient approach to improve the performance of inverted PSCs by introducing an inexpensive additive KBF_4 . With the addition of KBF_4 , the carrier lifetimes are prolonged in the perovskite layer, which can be attributed to the improved crystallinity, released lattice strain, and defect passivation by the additive. Consequently, a champion inverted device with a PCE of 23.04% is achieved while control devices without the additive only show the highest efficiency of 21.13%. Moreover, the device stability is increased by the additive. Therefore, this work provides a convenient approach to fabricate high-performance inverted PSCs.

2. Result and discussion

A one-step spin-coating method with chlorobenzene antisolvent washing is used to process the KBF_4 mixed $\text{Cs}_{0.05}(\text{FA}_{0.95}\text{MA}_{0.05})_{0.95}\text{Pb}(\text{I}_{0.95}\text{Br}_{0.05})_3$ film in this study as reported earlier.^[21,22] KBF_4 is employed with different molar ratios as additive to mix into perovskite precursor solutions. The detailed information for processing is described in the supporting information. Due to the similar ionic radius of BF_4^- (218 pm) and I^- , BF_4^- may enter into the perovskite lattice to replace I^- ions.^[23] Therefore, X-ray diffraction patterns (XRD) and X-ray photoelectron spectroscopy (XPS) were employed to determine the change in perovskite crystal lattice and chemical states. As shown in Figure 1a, no new peak can be observed in the XRD patterns after the addition of 1.5% KBF_4 , indicating that the introduction of KBF_4 does not lead to a new perovskite phase. Besides, the enhanced peak intensity indicates potentially better

perovskite texturing or crystallinity. The peaks of unreacted PbI_2 can be attributed to the extra stoichiometric ratio of PbI_2 , which is mainly for defects passivation at the grain boundaries of perovskite.^[24,25] Notably, as shown in Figure S2 (Supporting Information), some peaks (001, 002, 022) shift to smaller angles for 0.07 degree, indicating an expanded crystal lattice and larger lattice constants induced by the substitution of I^- with BF_4^- . In the XPS spectra shown in Figure 1b, the characteristic peak of F 1s can be observed at 693.49 eV in a perovskite thin film with 1.5% KBF_4 , while it is absent in a control sample without the additive. This result confirms the successful introduction of KBF_4 in the perovskite film. Besides, the characteristic peaks of Pb 4f at 138.77 eV ($4f_{7/2}$) and 143.63 eV ($4f_{5/2}$) shift to higher binding energy after the incorporation of KBF_4 due to the high electronegativity of F atoms, suggesting a potential interaction between Pb^{2+} and BF_4^- . The expanded lattice structure is attributed to the longer covalent bond between Pb^{2+} and BF_4^- . Although the ionic radius of BF_4^- is slightly smaller than I^- , the interaction between Pb^{2+} and BF_4^- is weaker than that between Pb^{2+} and I^- because the higher polarizability of I^- will facilitate the hybridization with Pb^{2+} and lead to a stronger interaction. Moreover, the spherical electron cloud of I^- is also conducive to hybridization as compared to the tetrahedral one of BF_4^- .^[26]

To investigate the impact of KBF_4 to the morphology of triple-cation mixed perovskite, the perovskite films were characterized under scanning electron microscopy (SEM). As showed in Figure 1d,e, the average grain size of the perovskite obviously increases after the addition of KBF_4 , which is clearly presented in the statistical graph of grain size (Figure 1f). The enhancement of the crystallinity can be attributed to slower

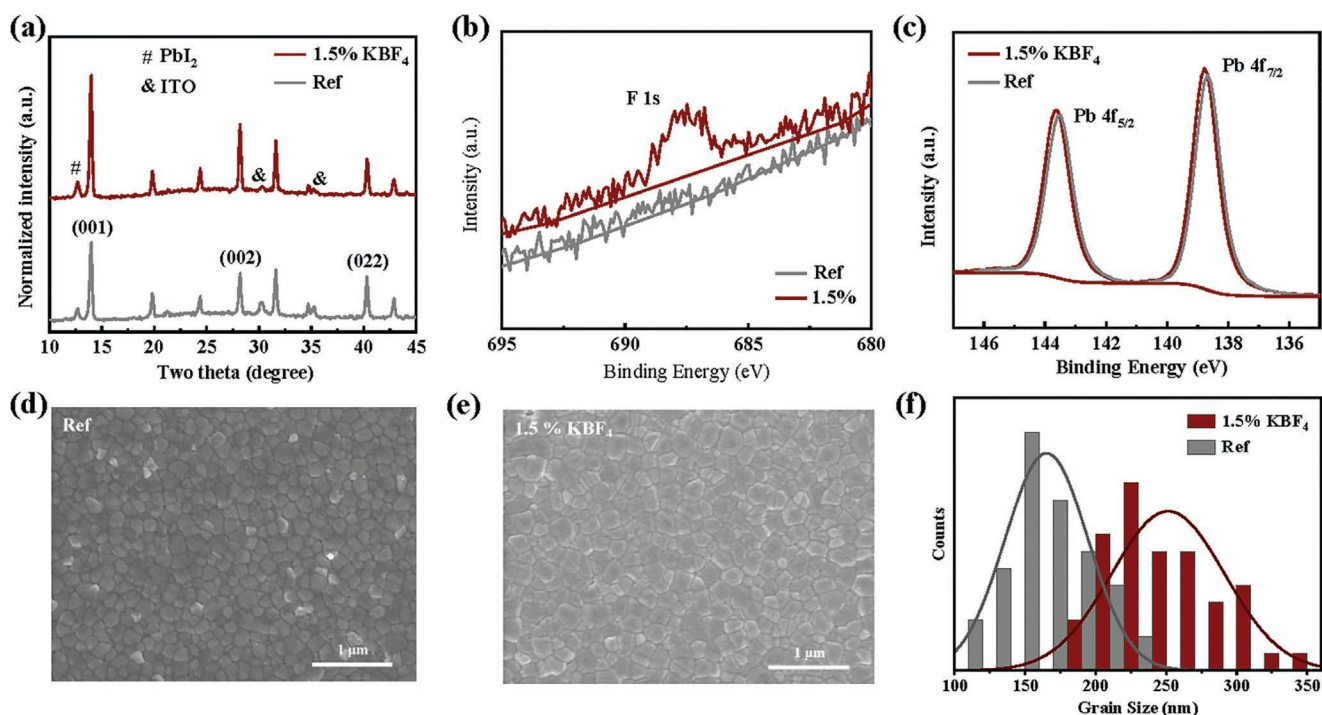


Figure 1. a) The XRD patterns of triple cation mixed perovskite with and without KBF_4 . b,c) XPS spectra of b) F 1s and c) Pb 4f for the perovskite films with and without KBF_4 . d,e) The plane-view SEM images of thin films with and without the addition of KBF_4 . f) The distribution of the grain size of perovskite with and without the addition of KBF_4 .

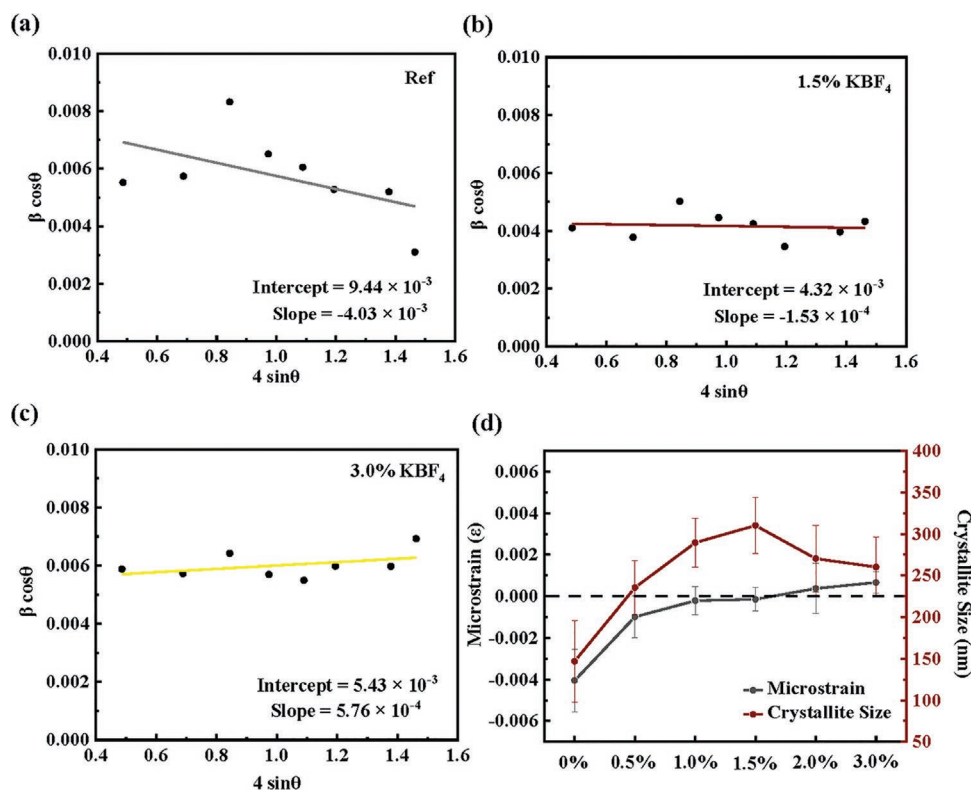


Figure 2. a–c) Williamson–Hall plots obtained from XRD patterns of perovskite thin films with different ratios of KBF_4 . d) The trend of microstrain and crystallite size obtained from fitted Williamson–Hall plots.

crystallization process due to increased Gibbs energy of perovskite nucleation with the incorporation of pseudo-halide ions into perovskite lattice.^[27] The resulting larger grain size can lead to reduced defect density and longer carrier lifetime that will be characterized in the later part. The roughness of perovskite thin films was then measured by Atomic Force Microscope (AFM), as shown in Figure S3 (Supporting Information). The roughness remained almost unchanged when 1.5% KBF_4 was added. However, it increased dramatically from 23.0 to 52.1 nm when 3.0% KBF_4 was added, indicating a degraded surface morphology.

Next, the quality of perovskite films was evaluated by Williamson–Hall analysis (Figure S4, Supporting Information). The grain size and microstrain of perovskite films can be evaluated from the XRD patterns quantitatively by the relationship plot of $\beta hkl \times \cos(\theta) = K\lambda/D + 4\epsilon \times \sin(\theta)$,^[14] where β is the full width half maximum (FWHM) of diffraction peaks, h , k , and l are the Miller index, K is the shape factor that is 0.9 for a cubic structure, λ is the wavelength of the incident X-rays and D is crystallite size. Microstrain of a perovskite film is strongly associated with compositional inhomogeneity. In addition, experimental conditions such as annealing temperature could have impact on it.^[28] Figure 2a–c shows the Williamson–Hall analysis based on the XRD patterns of the perovskites with different KBF_4 addition levels. The grain size and microstrain of the samples are summarized in Figure 2d. The control sample shows a negative (compressive) strain and small grain size of 150 nm. The lattice strain decreases and grain size increases after the introduction of KBF_4 and reach the lowest strain and the largest

grain size when 1.5 mol % of KBF_4 is added. However, more addition of KBF_4 leads to negative effect such as increased tensile strain and smaller grain size. Notably, the average grain size is only ≈ 150 nm in the control sample without KBF_4 while it is increased to ≈ 300 nm with 1.5 mol% of KBF_4 , which is consistent with the observation from SEM images shown in Figure 1f. Substituting FA^+ with smaller A sites (MA^+ or Cs^+) may distort P–I–Pb bonds thereby tilting the PbI_6 octahedron. One of the solutions is to introduce smaller and larger ions together, which is called strain-compensation strategy. In this case, the longer covalent bonds between BF_4^- between Pb^{2+} indicates larger effective radius and thus the introduction of BF_4^- can help balance the distorted lattice structure caused by the incorporation of smaller MA^+ and Cs^+ , leading to released strain and decreased defect density.

Next, the steady-state photoluminescence (PL) tests were performed on perovskite thin films with different ratios of KBF_4 . As shown in Figure 3a, the PL intensity of perovskite thin film increases after the introduction of KBF_4 and reaches the strongest intensity (790 nm) when 1.5% KBF_4 is applied. However, when extra amount of KBF_4 is added, the peak intensity decreases with the increase of addition level. Then, time-resolved photoluminescence (TRPL) was tested on the samples. The TRPL curves (Figure 3b) can be fitted with a biexponential decay equation:

$$I(t) = A_1 \exp\left(\frac{-t}{\tau_1}\right) + A_2 \exp\left(\frac{-t}{\tau_2}\right) + I_0 \quad (1)$$

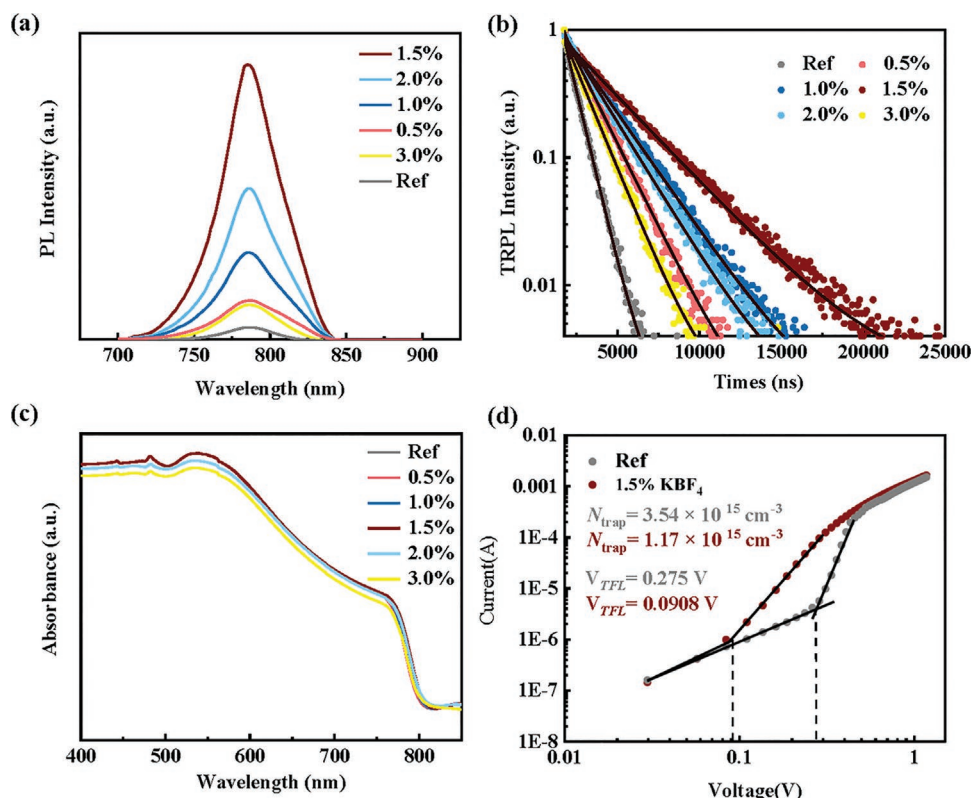


Figure 3. a,b) Steady-state and time-resolved PL of the perovskite thin film with different ratio of KBF₄. c) UV-vis absorbance and Tauc plot of perovskite thin film with different ratio of KBF₄. d) The curves of SCLC of the electron-only devices with a device structure of ITO/ SnO₂/ Perovskite/ PCBM/ Ag.

where τ_1 and τ_2 are the lifetimes of two decay components, A_1 and A_2 are coefficients of the two components and I_0 is a constant. The average lifetime is given by: $\tau_{\text{ave}} = \frac{\sum A_i \tau_i^2}{\sum A_i \tau_i}$, where τ_i is decay times and A_i is amplitudes.

As showed in Table 1, the trend of average lifetime (τ_{ave}) is consistent with the PL intensity. The τ_{ave} reaches the longest time when 1.5% KBF₄ is added, increasing from original 0.799 μs (control sample) to 3.24 μs . The greatly prolonged lifetimes indicate the reduced trap density and suppressed nonradiative recombination in perovskite thin films. However, the lifetimes decrease to 2.06 and 1.39 μs when the concentration further increases to 2.0% and 3.0%, respectively, which can be attributed to decreased grain size and bigger tensile strain in the films.

Table 1. The carrier lifetimes of perovskite thin films with different ratios of KBF₄.

	$\tau_1[\text{ns}]$	A_1	$\tau_2[\mu\text{s}]$	A_2	$\tau_{\text{ave}}[\mu\text{s}]$
Ref	16.1	0.220	0.799	0.840	0.799
0.5%	119	0.0601	1.65	0.882	1.65
1.0%	93.2	0.0275	2.35	0.837	2.35
1.5%	135	0.0384	3.24	0.772	3.24
2.0%	25.5	0.00387	2.06	0.867	2.06
3.0%	3.28	0.0723	1.39	0.837	1.39

The UV-vis light absorption spectra of the triple-cation mixed perovskite are then showed in Figure 3c. The perovskite thin films with relatively low concentration of KBF₄ show similar light absorption intensity with the control sample. The optical bandgap (E_g) calculated through Tauc plot $((\alpha h\nu)^2 - h\nu)$ are shown in Figure 3c, α , h , and ν were the absorption coefficient, Planck constant, and photofrequency, respectively. The bandgaps of the triple-cation perovskite with different concentrations are calculated to be ≈ 1.54 to 1.55 eV, indicating that KBF₄ leads to negligible impact to the bandgap of perovskite.

To quantitatively assess the defect density of the perovskite films, space charge limited current (SCLC) measurements based on electron-only device (ITO (Indium tin oxide)/SnO₂/Perovskite/PCBM/Ag) were conducted (Figure 3d). The defect density (N_{trap}) can be calculated from the trap-filling limit voltage (V_{TFL}) by:

$$N_{\text{trap}} = \frac{2V_{\text{TFL}}\epsilon\epsilon_0}{qL^2} \quad (2)$$

where L is the thickness of the perovskite film, q is the elementary charge, ϵ and ϵ_0 are the dielectric constants of perovskite and vacuum, respectively.^[29,30] The V_{TFL} calculated from the I - V curves of SCLC decreases from 0.275 to 0.0908 V. Consequently, the trap density of the perovskite film is reduced from 3.54×10^{15} to $1.17 \times 10^{15} \text{ cm}^{-3}$ when 1.5% KBF₄ is added. This result matches well with the prolonged carrier lifetime measured by TRPL, indicating that the incorporation of KBF₄ could

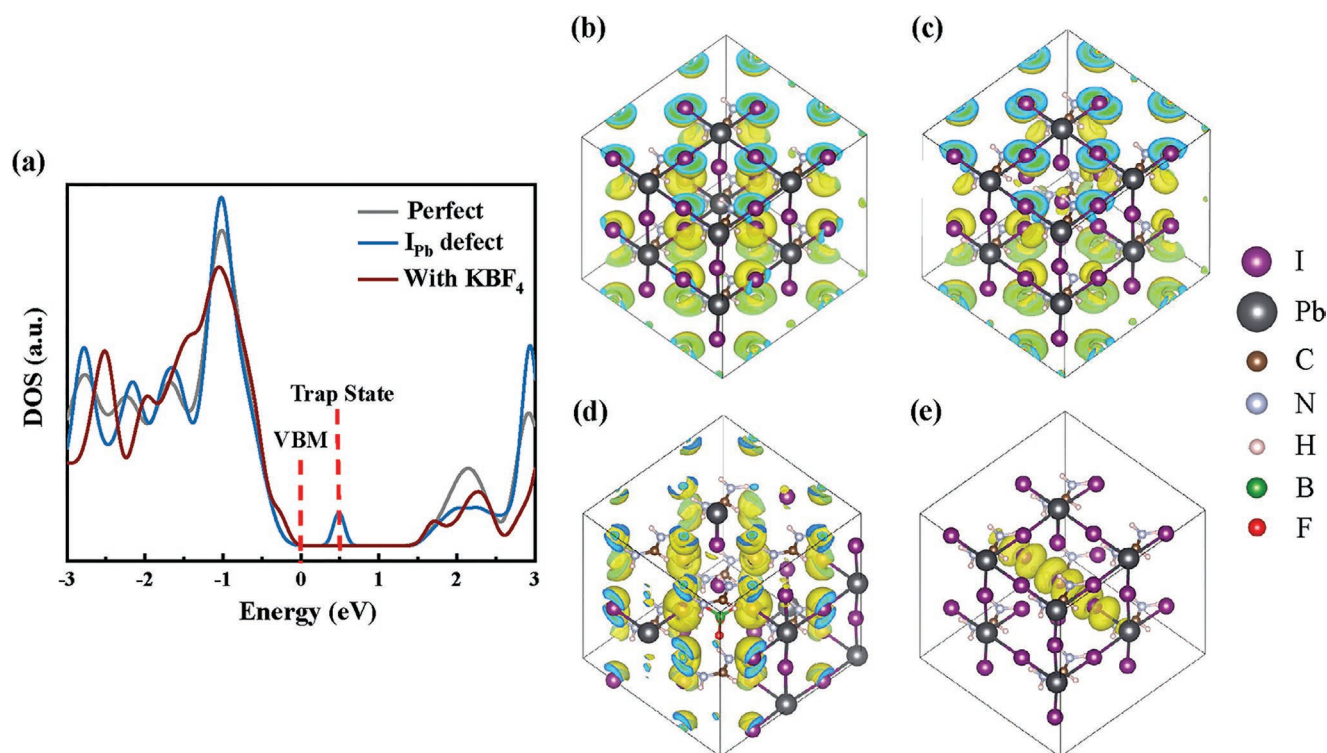


Figure 4. DFT calculations for different perovskite supercells. a) DOS of pristine FAPbI₃, FAPbI₃ with a I_{Pb} (Pb substituted by I) antisite defect, and FAPbI₃ with a I_{Pb} antisite defect with BF₄⁻ substitution of a nearby I⁻ ion. Simulated charge density distribution of b) pristine FAPbI₃, c) FAPbI₃ with a I_{Pb} (Pb substituted by I) antisite defect and d) FAPbI₃ with a I_{Pb} antisite defect with BF₄⁻ substitution of a nearby I⁻ ion at VBM, respectively. e) Simulated charge density distribution of FAPbI₃ with a I_{Pb} (Pb substituted by I) antisite defect at the deep state.

effectively reduce the defects in triple-cation mixed perovskite. This is achieved by releasing the strain in perovskite lattice as we have verified.

To have a deeper understanding on the defect passivation mechanisms of BF₄⁻ doped perovskite material, simulation of density-of-state (DOS) and charge density distribution based on density functional theory (DFT) are employed. To simplify the simulation, we calculated the defect passivation effect of replacing I⁻ with BF₄⁻ in a FAPbI₃ crystal, which is expected to be similar in triple-cation mixed perovskites because the interaction between BF₄⁻ and Pb²⁺/I⁻ plays a key role. It is well-known that antisite defects related to Pb and I are detrimental for carrier transport since those ions determine the band edge states and such defects tend to form deep traps as Shockley–Read–Hall (SRH) recombination centers.^[31–34] To demonstrate the influence of antisite defect on the electronic properties of perovskite and the passivation effect of BF₄⁻, the DOS and charge density distribution are simulated for the following structures: 1) 2 × 2 × 2 supercells of pristine FAPbI₃, 2) 2 × 2 × 2 supercells of FAPbI₃ with I_{Pb} (Pb substituted by I) antisite defect, 3) 2 × 2 × 2 supercells of FAPbI₃ with I_{Pb} antisite defect and BF₄⁻ substitution of a nearby I⁻ ion. **Figure 4a** compares simulated DOS of the three structures. The introduction of antisite defect induces a deep acceptor state near mid-gap, consistent with previous calculation.^[35] When BF₄⁻ ion is introduced near the defect, the deep state is replaced by a swallow state near valence band maximum (VBM), indicating the successful defect passivation of BF₄⁻. Such effect can be

attributed to the interactions between the electron-rich under-coordinated I⁻ ions with the electron-deficient fluorine atoms in BF₄⁻. To further demonstrate the passivation effect, charge density distributions for different scenarios are visualized (Figure 4b–e). Figure 4b–d shows charge density distribution at VBM in the three respective structures. The charge density is uniformly distributed throughout the cells at this energy level, indicating that the electrons are highly mobile and the swallow state induced by BF₄⁻ substitution will not cause charge density localization. However, the charge density becomes highly localized near the deep trap state for the defective cell without passivation (Figure 4e), which implies that such state can act as SRH recombination center. The passivation of such state by BF₄⁻ ions is therefore beneficial for carrier lifetime. Hence, the simulation gains more insight into the defect passivation effect of BF₄⁻ ions to perovskite thin film, further justifying the enhanced efficiency and stability of the resultant solar cells.

Next, we fabricated PSCs with the structure of ITO/PTAA/Cs_{0.05}(FA_{0.95}MA_{0.05})_{0.95}Pb(I_{0.95}Br_{0.05})₃/PCBM/BCP/Ag to investigate the impact of KBF₄ on the performance of PSCs (Figure S6, Supporting Information). The control devices without KBF₄ show the maximum PCE of 21.13%, *J*_{sc} of 24.90 mA cm⁻², *V*_{oc} of 1.12 V and *FF* of 0.75. Then, the PSC with different ratios of KBF₄ were fabricated. As shown in **Table 2**, the device performance increases with the introduction of KBF₄ and shows the best PCE of 23.04% when 1.5% KBF₄ is introduced. The champion device shows *J*_{sc} of 24.93 mA cm⁻², *V*_{oc} of 1.13 V and high *FF* of 0.82 (**Figure 5a**). However, the device performance

Table 2. The parameters of control device, champion device with different ratios of KBF₄. (30 samples for each condition).

Sample		J_{sc} [mA cm ⁻²]	V_{oc} [V]	FF	PCE [%]
Ref	Champion	24.90	1.120	0.76	21.13
	Average	24.65 ± 0.25	1.118 ± 0.003	0.75 ± 0.01	20.20 ± 0.92
0.5% KBF ₄	Champion	24.88	1.123	0.78	21.78
	Average	24.66 ± 0.22	1.118 ± 0.004	0.77 ± 0.01	20.90 ± 0.88
1.0% KBF ₄	Champion	24.95	1.125	0.80	22.45
	Average	24.67 ± 0.25	1.121 ± 0.003	0.79 ± 0.01	21.43 ± 0.95
1.5% KBF ₄	Champion	24.93	1.130	0.82	23.04
	Average	24.70 ± 0.23	1.127 ± 0.003	0.81 ± 0.01	22.45 ± 0.62
2.0% KBF ₄	Champion	24.85	1.123	0.77	21.58
	Average	24.58 ± 0.28	1.119 ± 0.005	0.76 ± 0.01	20.48 ± 0.97
3.0% KBF ₄	Champion	24.60	1.080	0.67	17.89
	Average	24.46 ± 0.22	1.080 ± 0.006	0.66 ± 0.01	16.93 ± 0.96

decreases when more KBF₄ is introduced. The J_{sc} , V_{oc} , and FF of the devices are decreased to 24.60 mA cm⁻², 1.08 eV and 0.67, respectively, when 3.0% KBF₄ is added. This trend is consistent with the result of PL measurement, which demonstrates that 1.5% KBF₄ delivers the longest carrier lifetime. The external quantum efficiency (EQE) of the devices and integrated J_{sc} are shown in Figure 5b, which are consistent with the values obtained from the J - V curves.

The detailed parameters of the PSCs are demonstrated in Figure 5c–f. As shown in the figure, the elevated performance of PSCs is mainly attributed to the greatly enhanced FF . The FF in a PSC is associated with the carrier transportation in the bulk of perovskite and interfaces. Low FF is generally caused by severe interfacial nonradiative recombination or low charge extraction efficiency between perovskite and transporting layers.^[36–39] Therefore, the introduction of KBF₄ can improve FF by reducing trap density and improving carrier lifetime as evidenced by the result of SCLC and TRPL. Moreover, K⁺ ions can modify the interface by forming KBr/KI with uncoordinated halides to passivate the grain boundaries.^[40,41] This KBr/KI solid complex not only prevent halides migration but also enhance electron extraction, which is favorable for device performance.^[42]

At the tail of EQE spectra in Figure 5b, the slope of the exponential EQE defines the Urbach energy (E_u), which is proportional to $\exp((E-E_G)/E_u)$ (Figure S5, Supporting Information).^[43,44] The E_u of the KBF₄-treated device is calculated to be 17.2 meV, which is slightly smaller than the control device of 18.8 meV. Lower Urbach energy generally indicates less defects in the perovskite layer. Thus, the lower E_u of KBF₄-treated device also suggests that KBF₄ can passivate defects in the film. Besides, the bandgaps calculated from EQE spectra were 1.54 eV for KBF₄-treated perovskite and 1.55 eV for control device, which matches well to the bandgap obtained from UV-vis absorption spectra.

To investigate the improvement in device stability, we demonstrated the thermal stability (Figure 5g), photostability (Figure 5h), and long-term storage stability (Figure 5i) tests on

our devices. The thermal stability test was carried out under 80 °C heating in N₂ atmosphere without encapsulation. In this work, the target device maintained over 90% efficiency after heating for 500 h while the control only kept 70% efficiency at the same condition. Besides, the photostability and long-term storage stability tests were also conducted in N₂ glovebox without encapsulation. It was found that the target device maintained over 89% and 97% efficiency respectively after continuous illumination and storage in inert atmosphere while the control device showed a much poor stability. In triple-cation perovskite, the MA⁺ may escape from the lattice due to its worse thermal stability, thereby leading to migration of uncoordinated halide ions and perovskite degradation. The ion migration is more serious under working conditions.^[26] In this case, the introduction of BF₄⁻ may release the lattice strain and thereby stabilize perovskite lattice. Apart from this, K⁺ ions can prevent the ion migrations by forming solid complex KBr/KI with uncoordinated halide ions at grain boundaries, thereby delivering more stable perovskite grain boundaries.^[45,46] Therefore, the combining benefits of BF₄⁻ and K⁺ contribute to the elevated device stability.

Considering the good performance of PSC achieved on inverted structure, we carried out our standard fabricating conditions on flexible PET (polyethylene glycol terephthalate) substrate, the structure of the device is composed of PET/PEDOT:PSS/PTAA/Perovskite/PCBM/BCP/Ag (Figure 6a). Transparent electrode PEDOT: PSS was prepared according to previous research,^[47] and an Au film is coated besides the PEDOT:PSS film as a conductor for the convenience of testing. As shown in Figure 6b, the flexible PSCs deliver PCE of 21.02%, J_{sc} of 25.08 mA cm⁻², V_{oc} of 1.06 V and FF of 0.79. The slightly increased J_{sc} is attributed to the higher transparency of PEDOT: PSS film as compared to ITO and matches well with the integrated J_{sc} from EQE (23.83 mA cm⁻², Figure 6c). Moreover, the flexible devices maintain 90% of the original PCE after bending for >1500 times at a bending radius of 8 mm (Figure 6d).

3. Conclusion

In summary, we have demonstrated that a small amount of KBF₄ is an effective additive to boost the performance of triple-cation mixed inverted PSCs. The champion device delivers a PCE of 23.03%, J_{sc} of 24.93 mA cm⁻², V_{oc} of 1.13 V and a high FF of 0.82. We find that KBF₄ can enhance the crystallinity and release microstrain in the perovskite films, which is favorable for the photovoltaic performance. Moreover, the trap density is reduced and nonradiative recombination is suppressed in the perovskite thin film due to defect passivation by BF₄⁻ in the bandgap. This work provides a convenient strategy to achieve high-performance PSCs with an inverted device structure, which is applicable for the fabrication of flexible, tandem, and large-area devices.

4. Experimental Section

Materials: Formamidinium iodide (99.99%) (FAI), methylammonium iodide (99.99%) (MAI), and Phenethylammonium iodide (99.99%)

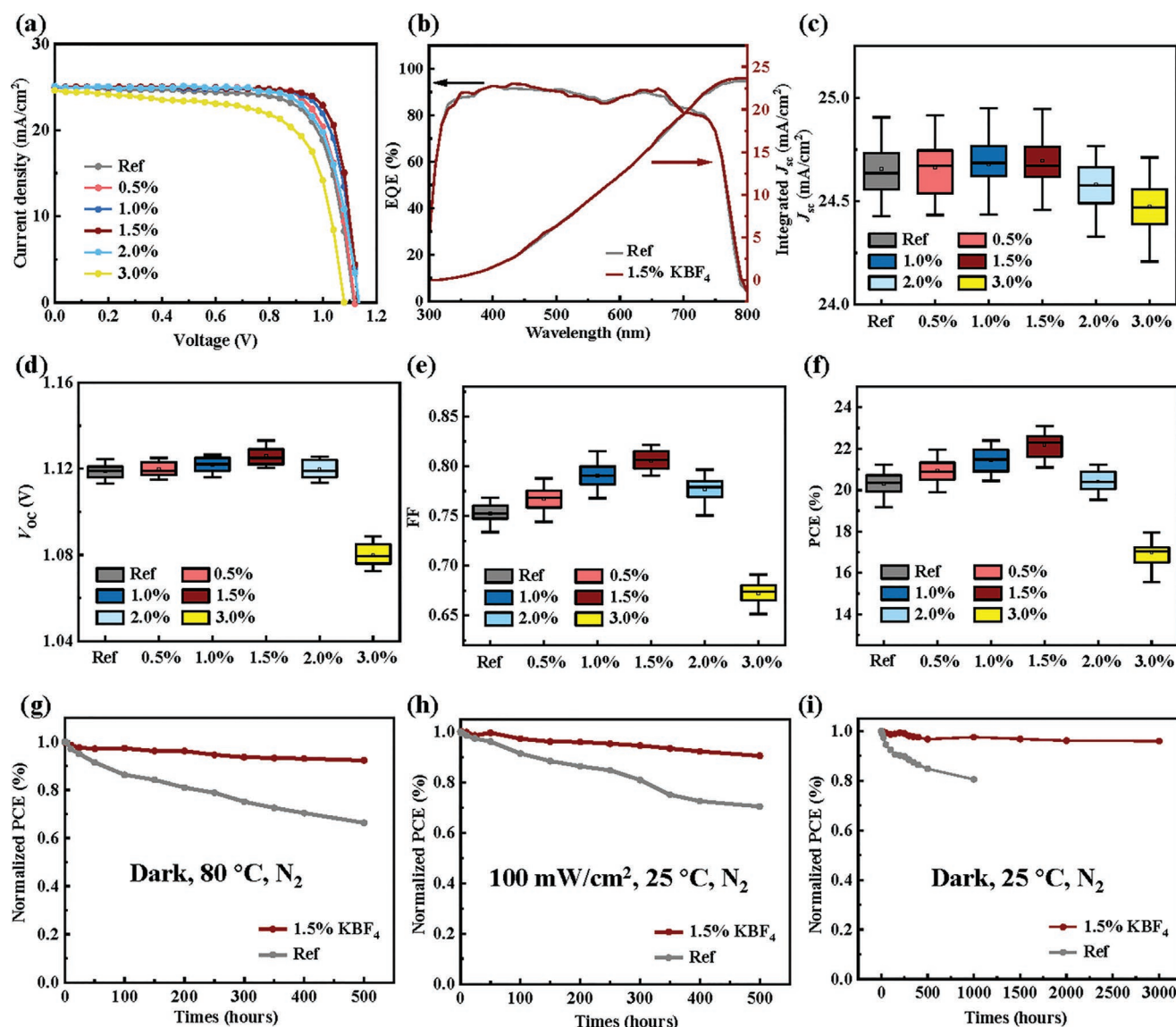


Figure 5. a) J–V curves of referential devices and champion devices with different molar ratio of KBF₄. Device area: 0.048 cm². b) The EQE spectra of the champion device and control device. c–f) Comparisons of photovoltaic performance parameters between referential devices and devices with different ratio of KBF₄. Thirty samples were measured for each condition. g) Thermal stability test under 80 °C heating in N₂ atmosphere without encapsulation. h) photostability stability test under the continuous illumination (100 mW cm^{−2}) in N₂ glovebox without encapsulation. i) Long-time storage stability under dark in N₂ atmosphere without encapsulation.

(PEAI) were purchased from Greatcell solar materials. Methylammonium bromide (99.99%) (MABr), Cesium (99.99%) (CsI), and Poly[bis(4-phenyl)(2,4,6-trimethylphenyl)amine] (Mn = 15000–25000) (PTAA) were purchased from Xi'an Polymer Light Technology Corp. (China). Iodide Lead iodide (99.99%) (PbI₂) and dimethylmethanamide (99.8%) (DMF) were obtained from Alfa Aesar Inc. N,N-dimethyl-sulfoxide (99.9%) (DMSO), chlorobenzene (99.9%) (CB), and 2,9-dimethyl-4,7-diphenyl-1,10-phenanthroline (96%) (BCP) were purchased from Sigma-Aldrich, Inc. Phenyl-C₇₁-butyric acid methyl ester (99%) (PCBM) was purchased from Nano-C, Inc. KBF₄ (99%) was purchased from BLD pharm, Inc. All chemicals were used as received without further purification.

Preparation of Triple Cation Mixed Perovskite Solution: The triple cation perovskite solution was prepared by mixing two 1.2 M FAPbI₃ and MAPbBr₃ perovskite solutions in DMF: DMSO (4:1 volume ratio, v: v) in a particular ratio (e.g., 95:5). The 1.2 M FAPbI₃ solution was thereby prepared by dissolving FAI (722 mg) and PbI₂ (2130 mg) in 2.8 mL DMF

and 0.7 mL DMSO that contains a 10 molar % excess of PbI₂. The 1.2 M MAPbBr₃ solution was made by dissolving MABr (470 mg) and PbBr₂ (1696 mg) in 2.8 mL DMF and 0.7 mL DMSO that contains a 10 molar % excess of PbBr₂. Last, 40 μL of a 1.5 CsI solution in DMSO (389 mg CsI in 1 mL DMSO) was mixed with 960 μL of the above-described mixture of FAPbI₃ and MAPbBr₃ resulting in a nominal perovskite stoichiometry of Cs_{0.05}(FA_{0.95}MA_{0.05})_{0.95}Pb(I_{0.95}Br_{0.05})₃, respectively.

Device Fabrication: To fabricate a device structure of glass/ITO/PTAA/Perovskite/PCBM/BCP/Ag, ITO glass substrates were ultrasonically cleaned by deionized (DI) water, acetone, and isopropanol for 15 min, respectively. Then, the cleaned ITO substrates were dealt with air plasma for 8 min before use. Then the substrates were transferred to N₂ glovebox. After the substrates were transferred into glovebox, poly(triarylamine) (PTAA) solution (2 mg mL^{−1}) was spin-coated at 5000 rpm for 30 s and annealed at 100 °C for 10 min. The substrates were cool down to room temperature before use. Perovskite precursor solutions (1.2 M)

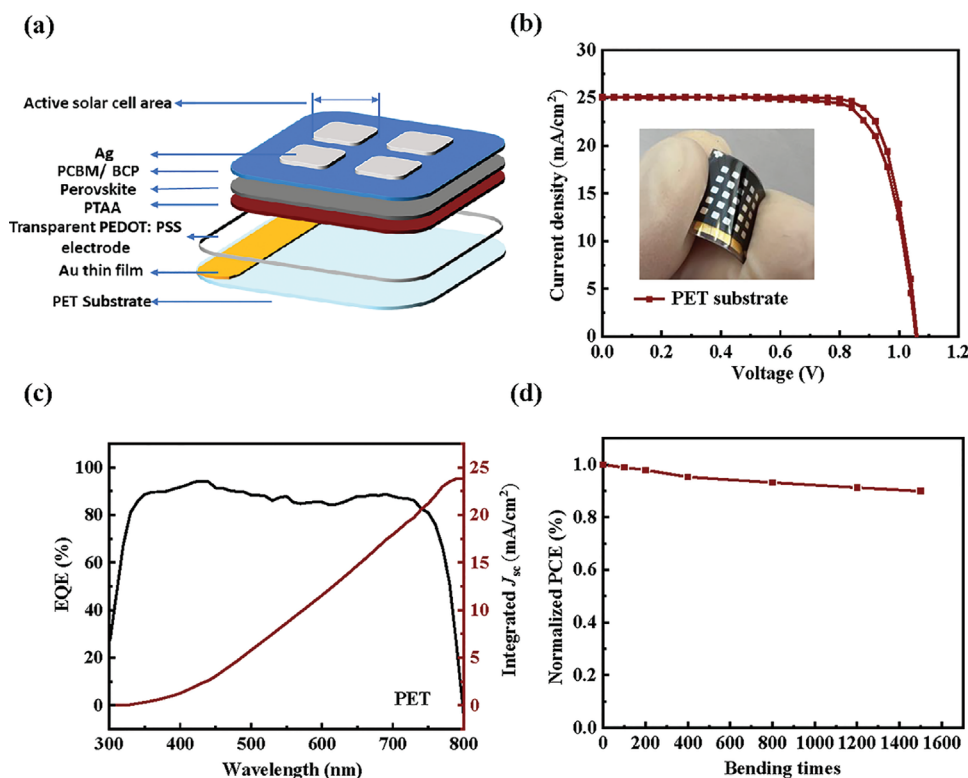


Figure 6. a) Flexible PSC with a device structure of PET/ PEDOT: PSS/ PTAA/ Perovskite/ PCBM/ BCP/ Ag. b) The J - V curves of a flexible PSC. Device area: 1 mm^2 . c) The EQE spectra of the flexible device. d) The bending stability of the flexible device.

were constructed by mixing FAI, PbI_2 , MABr, PbBr_2 , and CsI in DMF: DMSO mixed solvent with a chemical formula of $\text{Cs}_{0.05}(\text{FA}_{0.95}\text{MA}_{0.05})_{0.95}\text{Pb}(\text{I}_{0.95}\text{Br}_{0.05})_3$. The prepared precursor solution ($50 \mu\text{L}$) was spin-coated at 1000 rpm for 10 s and 5000 rpm for 30 s onto the PTAA-coated ITO substrate, $50 \mu\text{L}$ CB as antisolvent was dripped on the film at 10 s before the end of the last procedure and then annealed at 100°C for 30 min . Afterward, PCBM (20 mg mL^{-1}) and BCP (0.5 mg mL^{-1}) were spin-coated on the films at 1500 rpm for 60 s and 4500 rpm for 30 s , respectively. For solution with KBF_4 , different molar ratio of KBF_4 was added to the original 1.2 M FAPbI₃ solution. Finally, 200 nm silver electrodes were thermally evaporated onto the films at a chamber pressure of 10^{-7} Torr with a deposition rate of 0.5 \AA s^{-1} .

Characterization: J - V curves were measured by a Keithley 2400 source meter with a solar simulator under AM 1.5 G one sun illumination (Newport 66 902). The scanning rate was 100 mV s^{-1} with a voltage step of 10 mV . The EQE of the PSCs was obtained from an EQE system under DC mode. To reduce the optical reflection loss, an antireflection (AR) layer was added on the glass side during the test of the champion 5°C antisolvent treated devices. SEM images were measured by a field-emission SEM (Tescan MAIA3). XRD patterns were measured using $\text{Cu K}\alpha$ radiation (Rigaku, Smartlab) to analyze the crystallization of perovskite. PL was measured by the FLS 920 (Edinburgh Instruments, Ltd) with excitation at 645 nm .

Statistical Analysis: The data, figure, and statistical graph (J - V curves, XRD figures, XPS figures, Williamson-Hall plots, PL, UV-vis, SCLC, EQE, and stability tests) in the article is pre-processed and drawn by Origin Pro (ver. 2019). The SEM figure was processed by Digital Micrograph (ver. 3.4). The AFM figure was processed by NanoScope Analysis (ver. 1.7).

Computational Methods: All DFT simulations were conducted using Quantum Espresso (ver. 6.5).^[48] All the structures were fully relaxed before the DOS and charge density calculations. The relaxation was performed under Perdew, Burke, and Ernzerhof (PBE) exchange-correlation functionals^[49] with projector augmented wave (PAW)

method. The electronic convergence criterion was set to be $1 \times 10^{-6} \text{ eV}$. A plane wave basis set of 450 eV cut-off energy was used.

Supporting Information

Supporting Information is available from the Wiley Online Library or from the author.

Acknowledgements

H.C. and C.L. contributed equally to this work. This work was financially supported by the Research Grants Council (RGC) of Hong Kong, China (Project No. 15210319 and C5037-18G), Innovation and Technology Commission of Hong Kong, China (Innovation and Technology Fund – Guangdong-Hong Kong Technology Cooperation Funding Scheme (ITF-TCFS), Project No. GHP/042/19SZ), The Hong Kong Polytechnic University, Hong Kong, China (ZE2X and CD46), and Guangdong-Hong Kong-Macao Joint Laboratory for Photonic-Thermal-Electrical Energy Materials and Devices (GDSTC No. 2019B121205001).

Conflict of Interest

The authors declare no conflict of interest.

Data Availability Statement

The data that support the findings of this study are available in the supplementary material of this article.

Keywords

crystallinity, defects passivation, KBF₄, microstrains, Perovskite solar cells

Received: April 29, 2022

Revised: June 8, 2022

Published online:

- [1] Y. Rong, Y. Hu, A. Mei, H. Tan, M. I. Saidaminov, S. I. Seok, M. D. McGehee, E. H. Sargent, H. Han, *Science* **2018**, 361, 1214.
- [2] N. Li, X. Niu, Q. Chen, H. Zhou, *Chem. Soc. Rev.* **2020**, 49, 8235.
- [3] S. Tang, Y. Deng, X. Zheng, Y. Bai, Y. Fang, Q. Dong, H. Wei, J. Huang, *Adv. Energy Mater.* **2017**, 7, 1700302.
- [4] D. Luo, X. Li, A. Dumont, H. Yu, Z. H. Lu, *Adv. Mater.* **2021**, 33, 2006004.
- [5] S. Liu, Y. Guan, Y. Sheng, Y. Hu, Y. Rong, A. Mei, H. Han, *Adv. Energy Mater.* **2019**, 10, 1902492.
- [6] B. Chen, P. N. Rudd, S. Yang, Y. Yuan, J. Huang, *Chem. Soc. Rev.* **2019**, 48, 3842.
- [7] H. Min, D. Y. Lee, J. Kim, G. Kim, K. S. Lee, J. Kim, M. J. Paik, Y. K. Kim, K. S. Kim, M. G. Kim, T. J. Shin, S. Il Seok, *Nature* **2021**, 598, 444.
- [8] Y. L. Haizhou Lu, P. Ahlawat, A. Mishra, W. R. Tress, F. T. Eickemeyer, Y. Yang, F. Fu, Z. Wang, C. E. Avalos, B. I. Carlsen, A. Agarwalla, X. Zhang, X. Li, Y. Zhan, S. M. Zakeeruddin, L. Emsley, U. Rothlisberger, L. Zheng, A. Hagfeldt, M. Grätzel, *Science* **2020**, 370, 74.
- [9] A. M. Jaeki Jeong, M. Kim, J. Seo, H. Lu, Y. Yang, M. A. Hope, I. W. C. Yung Jin Yoon, B. P. D. J. H. Lee, B. W. A. Hagfeldt, M. Z. S., D. S. Kim, M. Grätzel, P. Ahlawat, T. E. F., S. J. u Choi, E. L., K. M., Y. Jo, J. Y. K. a., *Nature* **2021**, 592, 381.
- [10] H. W. K. Byung-wook Park, Y. Lee, D. o Y. Lee, M. G. Kim, G. Kim, K. i. j. Kim, Y. K. i Kim, J. Im, T. J. Shin, S. Il Seok, *Nat. Energy* **2021**, 6, 419.
- [11] C. Yi, J. Luo, S. Meloni, A. Boziki, N. Ashari-Astani, C. Grätzel, S. M. Zakeeruddin, U. Röthlisberger, M. Grätzel, *Energy Environ. Sci.* **2016**, 9, 656.
- [12] M. Saliba, T. Matsui, J. Y. Seo, K. Domanski, J. P. Correa-Baena, M. K. Nazeeruddin, S. M. Zakeeruddin, W. Tress, A. Abate, A. Hagfeldt, M. Grätzel, *Energy Environ. Sci.* **2016**, 9, 1989.
- [13] C. Dong, Z.-K. Wang, L.-S. Liao, *Energy Tech* **2020**, 8, 1900804.
- [14] H. M. Gwisu Kim, K. S. u Lee, *Science* **2020**, 370, 108.
- [15] W. G. Le Zhang, C.-j. Tong, X. Chen, *Sci. Rep.* **2018**, 8, 7760.
- [16] K. A. B. Nicholas Rolston, A. D. Printz, A. Gold-Parker, Y. Ding, M. F. Toney, M. D. McGehee, H. Dauskardt, *Adv. Energy Mater.* **2018**, 8, 1802139.
- [17] R. Wang, T. Huang, J. Xue, J. Tong, K. Zhu, Y. Yang, *Nat. Photo.* **2021**, 15, 411.
- [18] G. Tang, F. Yan, *Nano Today* **2021**, 39, 101155.
- [19] X. Lin, D. Cui, X. Luo, C. Zhang, Q. Han, Y. Wang, L. Han, *Energy Environ. Sci.* **2020**, 13, 3823.
- [20] Q. A. Matteo Degani, M. Albaladejo-Siguan, Y. J. Hofstetter, C. Cho, F. Paulus, G. Grancini, Y. Vaynzof, *Sci. Adv.* **2021**, 7, eabj7930.
- [21] E. Gutierrez-Partida, H. Hempel, S. Caicedo-Dávila, M. Raoufi, F. Peña-Camargo, M. Grischek, R. Gunder, J. Diekmann, P. Caprioglio, K. O. Brinkmann, H. Köbler, S. Albrecht, T. Riedl, A. Abate, D. Abou-Ras, T. Unold, D. Neher, M. Stolterfoht, *ACS Energy Lett.* **2021**, 6, 1045.
- [22] F. Li, X. Deng, F. Qi, Z. Li, D. Liu, D. Shen, M. Qin, S. Wu, F. Lin, S. H. Jang, J. Zhang, X. Lu, D. Lei, C. S. Lee, Z. Zhu, A. K. Jen, *J. Am. Chem. Soc.* **2020**, 142, 20134.
- [23] S. Nagane, U. Bansode, O. Game, S. Chhatre, S. Ogale, *Chem. Commun.* **2014**, 50, 9741.
- [24] D. H. Cao, C. C. Stoumpos, C. D. Malliakas, M. J. Katz, O. K. Farha, J. T. Hupp, M. G. Kanatzidis, *APL Mater.* **2014**, 2, 091101.
- [25] B. Shi, X. Yao, F. Hou, S. Guo, Y. Li, C. Wei, Y. Ding, Y. Li, Y. Zhao, X. Zhang, *J. of Physi. Chem. C* **2018**, 122, 21269.
- [26] J. Zhang, S. Wu, T. Liu, Z. Zhu, A. K. Y. Jen, *Adv. Func. Mater.* **2019**, 29, 1808833.
- [27] M. K. Kim, T. Jeon, H. I. Park, J. M. Lee, S. A. Nam, S. O. Kim, *Cryst. Eng. Comm.* **2016**, 18, 6090.
- [28] H.-S. Kim, N.-G. Park, *NPG A.Mater.* **2020**, 12, 12:78.
- [29] F. Zhang, S. Ye, H. Zhang, F. Zhou, Y. Hao, H. Cai, J. Song, J. Qu, *Nano Energy* **2021**, 89, 106370.
- [30] H. Zhang, S. Ye, Y. Hao, P. Zeng, J. Lian, J. Qu, J. Song, F. Zhang, *Chem. Eng. J.* **2022**, 445, 136803.
- [31] M. A. Green, A. Ho-Baillie, H. J. Snaith, *Nat. Photo.* **2014**, 8, 506.
- [32] Z. Xiao, Z. Song, Y. Yan, *Adv. Mater.* **2019**, 31, 1803792.
- [33] X. Wang, Y. Qiu, L. Wang, T. Zhang, L. Zhu, T. Shan, Y. Wang, J. Jiang, L. Kong, H. Zhong, H. Yu, F. Liu, F. Gao, F. Wang, C.-C. Chen, *Nano Energy* **2021**, 89.
- [34] T. J. Smart, H. Takenaka, T. A. Pham, L. Z. Tan, J. Z. Zhang, T. Ogitsu, Y. Ping, *J. Phys. Chem. Lett.* **2021**, 12, 6299.
- [35] N. Liu, C. Yam, *Phys. Chem. Chem. Phys.* **2018**, 20, 6800.
- [36] M. Stolterfoht, C. M. Wolff, Y. Amir, A. Paulke, L. Perdígón-Toro, P. Caprioglio, D. Neher, *Energy Environ. Sci.* **2017**, 10, 1530.
- [37] Q. Xue, Y. Bai, M. Liu, R. Xia, Z. Hu, Z. Chen, X.-F. Jiang, F. Huang, S. Yang, Y. Matsuo, H.-L. Yip, Y. Cao, *Adv. Energy Mater.* **2017**, 7.
- [38] X. Zhao, L. Tao, H. Li, W. Huang, P. Sun, J. Liu, S. Liu, Q. Sun, Z. Cui, L. Sun, Y. Shen, Y. Yang, M. Wang, *Nano Lett.* **2018**, 18, 2442.
- [39] D.-Y. Son, J.-W. Lee, Y. J. Choi, I.-H. Jang, S. Lee, P. J. Yoo, H. Shin, N. Ahn, M. Choi, D. Kim, N.-G. Park, *Nat. Energy* **2016**, 1, 16081.
- [40] L. Kuai, Y. Wang, Z. Zhang, Y. Yang, Y. Qin, T. Wu, Y. Li, Y. Li, T. Song, X. Gao, L. Wang, B. Sun, *Sol. RRL* **2019**, 3, 1900053.
- [41] F. Zheng, W. Chen, T. Bu, K. P. Ghiggino, F. Huang, Y. Cheng, P. Tapping, T. W. Kee, B. Jia, X. Wen, *Adv. Energy Mater.* **2019**, 9, 1901016.
- [42] T. Bu, J. Li, F. Zheng, W. Chen, X. Wen, Z. Ku, Y. Peng, J. Zhong, Y. B. Cheng, F. Huang, *Nat. Commun.* **2018**, 9, 4609.
- [43] X. Meng, J. Lin, X. Liu, X. He, Y. Wang, T. Noda, T. Wu, X. Yang, L. Han, *Adv. Mater.* **2019**, 31, 1903721.
- [44] S. Zhang, S. M. Hosseini, R. Gunder, A. Petsiuk, P. Caprioglio, C. M. Wolff, S. Shoaee, P. Meredith, S. Schorr, T. Unold, P. L. Burn, D. Neher, M. Stolterfoht, *Adv. Mater.* **2019**, 31, 1901090.
- [45] J. Cao, S. X. Tao, P. A. Bobbert, C. P. Wong, N. Zhao, *Adv. Mater.* **2018**, 30, 1707350.
- [46] M. Abdi-Jalebi, Z. Andaji-Garmaroudi, S. Cacovich, C. Stavrakas, B. Philippe, J. M. Richter, M. Alsari, E. P. Booker, E. M. Hutter, A. J. Pearson, S. Lilliu, T. J. Savenije, H. Rensmo, G. Divitini, C. Ducati, R. H. Friend, S. D. Stranks, *Nature* **2018**, 555, 497.
- [47] X. Fan, W. Nie, H. Tsai, N. Wang, H. Huang, Y. Cheng, R. Wen, L. Ma, F. Yan, Y. Xia, *Adv. Sci.* **2019**, 6, 1900813.
- [48] P. Giannozzi, S. Baroni, N. Bonini, M. Calandra, R. Car, C. Cavazzoni, D. Ceresoli, G. L. Chiarotti, M. Cococcioni, I. Dabo, A. Dal Corso, S. de Gironcoli, S. Fabris, G. Fratesi, R. Gebauer, U. Gerstmann, C. Gougoussis, A. Kokalj, M. Lazzeri, L. Martin-Samos, N. Marzari, F. Mauri, R. Mazzarello, S. Paolini, A. Pasquarello, L. Paulatto, C. Sbraccia, S. Scandolo, G. Sclauzero, A. P. Seitsonen, et al., *J. Phys. Condens. Matter* **2009**, 21, 395502.
- [49] K. Burke, J. P. Perdew, M. Ernzerhof, *Phys. Rev. Lett.* **1996**, 77, 3865.